



**Untangling the role of the carbon matrix in the magnetic coupling of Ni@C nanoparticles with mixed FCC/HCP crystal structures**

Journal:	<i>Journal of Materials Chemistry C</i>
Manuscript ID	TC-ART-01-2023-000257
Article Type:	Paper
Date Submitted by the Author:	20-Jan-2023
Complete List of Authors:	Fadel, Mona; University of Oviedo, Physics Martín-Jimeno, Francisco; INCAR Fernandez, Maria Paz; University of Oviedo, Physics Suárez-García, Fabián; Instituto Nacional del Carbón, INCAR-CSIC, Materials Chemistry Paredes, Juan; Instituto Nacional del Carbon, CSIC, Belo, Joao; IFIMUP Araujo, Joao; IFIMUP, Adawy, Alaa; Universidad de Oviedo, Unit of Electron Microscopy and Nanotechnology Martínez-Blanco, David; University of Oviedo, Servicios Científico-Técnicos Alvarez-Alonso, Pablo; Universidad de Oviedo, Physics Blanco, Jesus; University of Oviedo, Physics; Gorria, Pedro; University of Oviedo, Physics

# Journal of Materials Chemistry C

Materials for optical, magnetic and electronic devices

## Guidelines for Reviewers

Thank you very much for agreeing to review this manuscript for [Journal of Materials Chemistry C](#).



*Journal of Materials Chemistry C* is a weekly journal in the materials field. The journal is interdisciplinary, publishing work of international significance on all aspects of materials chemistry related to applications in optical, magnetic and electronic devices. Articles cover the fabrication, properties and applications of materials.

*Journal of Materials Chemistry C*'s Impact Factor is **8.067** (2021 Journal Citation Reports®)

---

*The following manuscript has been submitted for consideration as a*  
**FULL PAPER**

---

For acceptance, a Full paper must report primary research that demonstrates significant **novelty and advance**, either in the chemistry used to produce materials or in the properties/ applications of the materials produced. Work submitted that is outside of these criteria will not usually be considered for publication. The materials should also be related to the theme of optical, magnetic and electronic devices.

When preparing your report, please:

- Focus on the **originality, importance, impact** and **reproducibility** of the science.
- Refer to the **journal scope and expectations**.
- **State clearly** whether you think the article should be accepted or rejected and give detailed comments (with references) both to help the Editor to make a decision on the paper and the authors to improve it.
- **Inform the Editor** if there is a conflict of interest, a significant part of the work you cannot review with confidence or if parts of the work have previously been published.
- **Provide your report rapidly** or inform the Editor if you are unable to do so.

Best regards,

**Professor Natalie Stingelin**

Editor-in-Chief

Georgia Institute of Technology, USA

**Dr Michaela Mühlberg**

Executive Editor

Royal Society of Chemistry

Contact us

Please visit our [reviewer hub](#) for further details of our processes, policies and reviewer responsibilities as well as guidance on how to review, or click the links below.



What to do  
when you  
review



Reviewer  
responsibilities



Process &  
policies



January 20, 2023

Dear editor,

On behalf of my colleagues, I am very glad to submit this manuscript entitled **“Untangling the role of the carbon matrix in the magnetic coupling of Ni@C nanoparticles with mixed FCC/HCP crystal structures”** for consideration in **Journal of Materials Chemistry C**.

We have synthesized a nickel-imidazole-based metal-organic framework (MOF) by a simple method in aqueous medium at moderate temperature (95 °C), which allows to obtain a carbon-supported material through the carbonization of the MOF at different temperatures between 400 and 600 °C. The final product is a hybrid material containing Ni nanoparticles with “artichoke-like” morphology consisting of a Ni-FCC core and surrounding “bracts” of Ni-HCP and Ni<sub>3</sub>C. In addition, this synthesis procedure favours the formation of crystalline layers of turbostratic carbon covering most of the nanoparticles, which protect them against oxidation.

The mixture of those Ni-containing phases gives rise to a complex evolution of the physical-chemical behaviour with carbonization temperature. There is a growing interest in the investigation of Ni@C nanoparticles due to a variety of potential applications (i.e.: from catalysis to electromagnetic absorbers), and therefore, a precise understanding of the role played by the carbon atoms is of paramount importance in these systems. Frequently, FCC-Ni, HCP-Ni and Ni<sub>3</sub>C crystalline phases coexist in the samples, thus affecting the magnetization of Ni@C nanoparticle systems, but the true magnetic character of both HCP-Ni and Ni<sub>3</sub>C is still controversial [see for example: Carbon 167 (202) 364; *ibid.* 185 (2021) 477].

In our work, we have performed a joint analysis combining X-ray diffraction and electron microscopy together with magnetometry techniques, which permitted us to explain the formation and transformation of these different Ni-based crystalline phases along the synthesis process, including Ni<sub>3</sub>C and Ni with both hexagonal and cubic crystalline structures. We give clear evidence that the presence of carbon atoms are indeed far more relevant for understanding the physical behaviour of these Ni@C samples than previously thought.

We look forward to your feedback about our manuscript.

Yours sincerely,

Prof. Pedro Gorria

# Untangling the role of the carbon matrix in the magnetic coupling of Ni@C nanoparticles with mixed FCC/HCP crystal structures

Received 00th January 20xx,  
Accepted 00th January 20xx

DOI: 10.1039/x0xx00000x

Mona Fadel,<sup>a</sup> F. Julián Martín-Jimeno,<sup>b</sup> M.P. Fernández-García,<sup>a</sup> Fabián Suárez-García,<sup>b</sup> Juan Ignacio Paredes,<sup>b</sup> J. H. Belo,<sup>c</sup> J. P. Araújo,<sup>c</sup> Alaa Adawy,<sup>d</sup> David Martínez-Blanco,<sup>e</sup> Pablo Álvarez-Alonso,<sup>a,f</sup> Jesús A. Blanco<sup>a</sup> and Pedro Gorria<sup>\*a,f</sup>

Nowadays, Ni@C nanostructured materials are attracting a great deal of attention due to their multiple catalytic or magnetic functionalities. In this article we report on the investigation of the correlation between microstructure and magnetic properties of Ni nanoparticles embedded in a carbon matrix. The samples were obtained following a two-step procedure that ensures protection against nanoparticle oxidation, and was carried out in the following way: i) the synthesis of a nickel-imidazole-based metal-organic framework (MOF) by a simple method in aqueous medium at moderate temperature (95 °C); and ii) carbonization of the MOF at different temperatures between 400 and 600 °C to obtain a carbon-supported hybrid material, containing Ni nanoparticles with “artichoke-like” morphology, where a Ni-FCC core is surrounded by “bracts” of Ni-HCP and Ni<sub>3</sub>C. The average size of the nanoparticle slightly changes from 7 to 10 nm as the carbonization temperature is increased, but the Ni-FCC core diameter ranges from 3 to around 6 nm. We show how the information obtained from the evolution of the magnetic behaviour with carbonization temperature, X-ray diffraction and electron microscopy, complements each other by providing consistent structural and magnetic characteristics of the investigated Ni@C nanoparticles. In fact, this joint analysis allows us to explain the formation and transformation of different Ni-based crystalline phases along the synthesis process, including Ni<sub>3</sub>C and Ni with both hexagonal and cubic crystalline structures. The amount of conventional Ni-FCC is below 10 wt.% for the sample treated at 400 °C and can reach up to 50 wt.% for that of 600 °C. Finally, based on our current findings we propose an explanation for understanding the magnetic properties of Ni@C, in which the Ni-FCC core spins mainly govern the magnetic coupling of the whole system.

## Introduction

Nickel nanoparticles are intensively investigated because their physical-chemical properties make them highly attractive for several key applications, such as anode soil fuel cells, conductivity electrolytic layers, automotive catalytic converters, propellant and sintering additives, biocompatible antibacterial agents, magnetic separation, magnetic fluid and catalysts, or electromagnetic absorbers for applications in telecommunication technologies [1-7].

In the field of transition metal catalysis, nickel has several oxidation states and might be seen just as the younger and low-cost sibling of palladium or platinum as it lies just above them in the periodic table and thus, can readily perform many of the same elementary reactions as Pd and Pt. However, the catalytic activity of Ni is reduced, and its industrial applications are limited when it forms large aggregates. Therefore, it is interesting to follow strategies that allow the formation of small Ni clusters or nanoparticles (NPs) [8, 9], and more importantly, obtain them in supported matrices that prevent their aggregation. Owing to their unique properties, carbon supports are specially interesting among other support options, because they provide low density, small weight, high chemical and

thermal stabilities, and tuneable porous texture. Therefore, heterogeneous carbon catalysts were obtained through supporting Ni NPs on graphene, porous carbons and carbon nanotubes, etc [3, 10, 11].

In this regard, an original strategy towards carbon-supported Ni NPs is to obtain sacrificial materials based on metal-organic frameworks (MOFs), which then give rise to a large content of highly dispersed metallic NPs upon heat treatment (carbonization) [12]. During the last decade some works have reported MOFs containing metallic ions or clusters, synthesized and pyrolyzed at high temperature to trigger thermal decomposition of MOFs, thus providing metal or metal-oxide/C nanohybrids [13-15]. However, there are only few examples in the literature of Ni-containing MOFs that have been pyrolyzed to produce Ni@C catalysts after short reaction times (<30 min), moderate temperatures (95°C) and following environmental-friendly routes. Recently, a two-step procedure towards carbon-supported Ni NPs that fulfils those requirements was developed and relies on a simple aqueous synthesis of a MOF and its subsequent carbonization strategy [16]. It should be noted that this Ni-based MOF was named NiOF by analogy with zeolitic imidazolate frameworks (ZIF) because Ni acts as the coordinating metal and imidazolate as the ligand. In the first step of the procedure, NiOF itself was synthesized, whereas in the second step Ni NPs embedded in carbon matrices were obtained by carbonization. During the carbonization process different Ni-based crystalline phases are found: Ni<sub>3</sub>C, hexagonal close-packed (HCP) and face-centred cubic (FCC) crystal structures [16].

As is well known a face-centred cubic crystalline structure is the stable phase of nickel (Ni-FCC, PDF 03-065-2865) at ambient pressure and at temperatures up to its melting point (1726 K).

<sup>a</sup> Departamento de Física, Universidad de Oviedo, E-33007 Oviedo, Spain.

<sup>b</sup> Instituto de Ciencia y Tecnología del Carbono, INCAR-CSIC, C/Francisco Pintado Fe 26, 33011 Oviedo, Spain.

<sup>c</sup> IFIMUP, Departamento de Física e Astronomia da Faculdade de Ciências da Universidade do Porto, Rua do Campo Alegre, 687, 4169-007 Porto, Portugal.

<sup>d</sup> Unidad de Microscopía Electrónica y Nanotecnología, SCTs, Universidad de Oviedo, 33006 Oviedo, Spain.

<sup>e</sup> Unidad de Difracción de rayos X, SCTs, Universidad de Oviedo, 33006 Oviedo, Spain.

<sup>f</sup> IUTA, EPI, Universidad de Oviedo, 33203 Gijón, Spain.

However, the addition of small amount of light elements, such as N, C, B or H, can stabilize the hexagonal closed-packed crystalline structure (Ni-HCP, JCPDS file no. 45-1027) [17]. Theoretical predictions provide lattice parameter values for Ni-HCP of  $a = 2.500 \text{ \AA}$  and  $c = 3.980 \text{ \AA}$  [18], similar to those reported for a Ni-HCP phase obtained during the thermal decomposition of  $\text{Ni}_3\text{C}$  NPs ( $a = 2.496 \text{ \AA}$  and  $c = 4.078 \text{ \AA}$ ) [19], although some other works give values of  $a = 2.648\text{--}2.660 \text{ \AA}$  and  $c = 4.328\text{--}4.339 \text{ \AA}$  [20, 21]. The latter values are close to those of  $\text{Ni}_3\text{C}$  in either rhombohedral (JCPDS file no. 77-0194) or HCP (JCPDS file no. 04-0853) crystal structures,  $a \approx 2.6 \text{ \AA}$  and  $c \approx 4.3 \text{ \AA}$  [22]. Moreover, it was reported that the close packed crystal structure of  $\text{Ni}_3\text{C}$  could be described by either a hexagonal unit cell or otherwise by a rhombohedral supercell with  $a = \sqrt{3} a_{\text{HEX}}$  and  $c = 3 c_{\text{HEX}}$  [23, 24]. Consequently, it is extremely difficult to distinguish both phases, Ni-HCP and  $\text{Ni}_3\text{C}$ , by X-ray diffraction because the differences in the lattice spacing between Ni-HCP and rhombohedral  $\text{Ni}_3\text{C}$  phases are about  $10^{-2} \text{ \AA}$ , and even smaller for Ni-HCP and  $\text{Ni}_3\text{C}$ -HCP ( $10^{-3} \text{ \AA}$ ) [25].

To address this issue, some studies approached it from the magnetic point of view, reporting different Ni@C phases within the nanometer length-scale exhibiting diverse magnetic behaviour, which depends strongly on the synthesis procedure [26–30]. Although, Ni-HCP was theoretically predicted to exhibit ferromagnetic behaviour with a magnetic moment value close to that of Ni-FCC ( $0.59\text{--}0.76 m_{\text{B}}$  or  $56.1\text{--}72.3 \text{ emu/g}$ ) [28, 29], other experimental works claimed for nonmagnetic [30], antiferromagnetic [21], or even weakly ferromagnetic [31, 32] behaviour in Ni-HCP. Moreover, it was suggested that the weak magnetism of Ni-HCP may be triggered by  $\text{Ni}_3\text{C}$ , which was mistakenly identified as Ni-HCP [25]. However, the observation of a tiny magnetic signal in  $\text{Ni}_3\text{C}$  [22, 23, 33], that is assumed as a non-magnetic phase [23, 34, 35], could be ascribed to small Ni-FCC impurities [24, 34]. In summary, a consistent and comprehensive explanation of the discrepancies between theory and experiments concerning to the magnetic behaviour of Ni@C hybrid nanocomposites is still lacking.

In the present paper, we have performed a detailed experimental investigation into Ni@C NPs obtained via an environmentally friendly synthesis method at temperatures between 400 and 600 °C. We intend to shed light on the evolution of the different Ni-containing phases that are formed depending on the synthesis conditions (Ni-FCC, Ni-HCP and  $\text{Ni}_3\text{C}$ ) and at the same time, reveal the true magnetic character of Ni-HCP and  $\text{Ni}_3\text{C}$ . For this purpose, we have thoroughly analysed the crystal structure, morphology and magnetic properties by means of different structural and physical characterization methodologies including X-ray diffraction (XRD), high resolution transmission electron microscopy (HRTEM) and magnetometry.

## Experimental methods

### Synthesis procedure

Nickel acetate tetrahydrate ( $\text{Ni}(\text{OAc})_2 \cdot 4\text{H}_2\text{O}$ ) from Alfa Aesar and 2-methylimidazole (2-mIm) from Acros Organics were used

as starting materials. The samples were obtained following the two-step procedure to obtain Ni@C catalysts, as previously reported in Ref. [16]. Basically, it consists of: i) the synthesis of a nickel-imidazole MOF (NiOF) by a simple method in aqueous medium and ii) a thermal treatment at different carbonization temperatures to obtain a hybrid material formed by Ni NPs embedded in a carbon matrix.

Initially, 10 g of 2-mIm and 20 g of NiOAc were dissolved separately in 2 volumes of 50 ml of distilled water. The molar ratio between the reactants was  $[2\text{-mIm}]:[\text{NiOAc}] = 6:1$ . Secondly, both solutions were pre-heated separately at 95 °C, stirred, and purged under an Ar flow to avoid the surface oxidation of the formed material. Then, the NiOAc solution was poured into the 2-mIm solution, and the reaction occurs immediately, giving rise to the formation of the nickel-imidazole complex, as evidenced by a colour change (from green to yellow-orange). After 30 min under vigorous stirring at 95 °C, the reaction was stopped by introducing the solution in an ice-bath. The formed powder was recovered after washing with distilled water by centrifugation until no coloration was observed in the supernatant. The obtained metal-organic framework (NiOF) was dried under vacuum for 6 h at 200 °C to remove the residues of the non-reacted 2-mIm molecules that occluded the pores of the material. Finally, the NiOF samples were heated in a horizontal tubular furnace with  $\text{N}_2$  flux (99.999% purity) under a heating rate of  $5 \text{ }^\circ\text{C}\cdot\text{min}^{-1}$ . The heating temperatures were  $T = 400, 450, 500, 550$  or  $600 \text{ }^\circ\text{C}$  and accordingly, the samples are labelled hereafter as S400, S450, S500, S550, and S600, respectively.

### Materials characterization

The Ni content of the samples was determined by thermogravimetric analysis (TGA) using a SDT Q600 device (TA Instruments). Room temperature X-ray powder diffraction (XRD) patterns were collected in the  $35^\circ - 100^\circ 2\theta$  range using a PANalytical X'Pert Pro diffractometer in a Bragg-Brentano geometry using  $\text{Cu K}\alpha$  radiation ( $1.5406 \text{ \AA}$ ). A  $\text{LaB}_6$  standard has been used for calibration purposes. The Rietveld refinement of the diffraction patterns has been performed using the FULL-PROF package [36] and following the procedure developed in Ref. [37] for nanostructured systems. Microstructural analysis was performed based on the parameters obtained during the Rietveld refinement. The fit was carried out using a Thompson-Cox-Hasting function describing the shape of the diffraction peaks, and to obtain information about the size and strain of the crystallites, we have used a generalized Scherrer-peak-broadening formula [37].

TEM and HRTEM images were recorded using a JEOL 200-EXII and a JEOL-JEM-2100F microscopes operating at 180 kV and 200 kV, respectively. The sample specimens were prepared by dispersing and sonicating a small amount of the powdered sample in ethanol. Afterwards, several drops of the resulting suspension were placed on Cu TEM grids with ultrathin carbon films, and finally the solvent was allowed to evaporate. After evaluating several TEM micrographs, the diameters of randomly selected particles (at least 300 from each sample) were estimated with ImageJ software [38], to build the particle-size

histograms and fit them using a log-normal distribution. Besides, interplanar distances were obtained from the HRTEM images or their fast-Fourier-transform (FFT) [39, 40].

The temperature and magnetic field dependences of magnetization,  $M(T)$  and  $M(H)$  curves, were measured in a Quantum Design PPMS-14T platform equipped with a vibrating sample magnetometer (VSM) option at the University of Oviedo, and a MPMS 3 SQUID magnetometer placed at the Instituto de Física dos Materiais da Universidade do Porto (IFIMUP). The magnetization vs temperature measurements were performed following conventional zero-field-cooling (ZFC) and field cooling (FC) procedures, to obtain the corresponding  $M_{ZFC}(T)$  and  $M_{FC}(T)$  curves, respectively. Firstly, the samples were cooled down from 300 K to 10 K in zero field, then a magnetic field (100 Oe) was applied and kept constant during the measurement of the  $M_{ZFC}(T)$  curve on heating from 10 to 300 K. Subsequently, the  $M_{FC}(T)$  curve was measured under the same value of the applied magnetic field on cooling down from

300 K to 10 K. In addition, the isothermal magnetization as a function of applied magnetic field,  $M(H)$  curves, were collected at 5 K and 300 K in the  $\pm 55$  kOe applied magnetic field range.

## Results and discussion

### TGA measurements

In Table 1 we show the results of the thermogravimetric analysis carried out under an air flow with the aim of determining the Ni content. The percentage of Ni increases progressively with the carbonization temperature from 38.3 wt.% (S400 sample) to  $\approx 49 - 50$  wt.% (S550 and S600 samples). This increase is due to the progressive loss of volatile matter from the carbonaceous fraction taking place during the carbonization process, where the degree of polycondensation and aromatization of the carbon framework increases with temperature.

Table 1. Nickel percentage derived from TGA measurements and values for the structural parameters obtained from TEM and XRD data. Note that the number in parentheses is the estimated error, except for the NP size that correspond to the standard deviation (TEM).

Sample	TGA (wt.% Ni)	$D_{TEM}(\sigma)$ (nm)	$Ni_3C$ wt.%	Ni-FCC wt.%	Ni-FCC a (Å)	Ni-HCP wt.%	Ni-HCP a (Å) / c (Å)
S400	38	7 (6)	46 (5)	10 (2)	3.530	44 (5)	2.53 / 3.59
S450	45	8 (3)		64 (4)	3.523	36 (3)	2.49 / 4.10
S500	48	7 (2)		67 (4)	3.523	33 (3)	2.49 / 4.10
S550	50	8 (2)		78 (5)	3.524	22 (3)	2.49 / 4.11
S600	49	10 (6)		75 (5)	3.524	25 (3)	2.49 / 4.11

### Crystalline structure

Figure 1 shows the room temperature XRD patterns of the samples together with the fits. All of them exhibit Bragg reflections associated with the FCC ( $Fm\bar{3}m$ ) and HCP ( $P6_3/mmc$ ) crystal structures of Ni, and the relative change of the intensities are related to the percentage of these phases that evolve with the carbonization temperature.

As is well known, the difference between the FCC and HCP crystal structures lies in the way that successive hexagonal layers are stacked upon one another in both structures. Therefore, as was anticipated above, there is an important overlapping of Bragg diffraction peaks associated with these crystal structures. In fact, the peaks observed at around  $44^\circ$ ,  $76^\circ$  and  $93^\circ$  in  $2\theta$  are related to (111)/(002), (220)/(110) and (311)/(112) for Ni-FCC/Ni-HCP, respectively. Only using the Rietveld refinement method, we can separate both contributions refining the theoretical line profile due to both contributions until it matches the measured diffraction profile. Consequently, from the Rietveld analysis of the XRD patterns the percentage for the Ni-HCP phase decreases from 44 wt.% (S400) to 25 wt.% (S600), while the percentage of Ni-FCC grows from c.a. 10 wt. to 75 wt.% for the same samples (see Table 1). Note that these phase-content values are related to the crystalline phases discriminated by XRD.

If we focus our attention on the XRD pattern of sample S400, apart from those belonging to Ni-FCC and Ni-HCP other

reflections that can be ascribed to a nickel-carbide phase,  $Ni_3C$ , with either rhombohedral ( $R\bar{3}c$ ) and hexagonal ( $P6_3/mmc$ ) crystal structures have been identified. The value for the cell parameters of this  $Ni_3C$  phase ( $a = 4.515$  Å,  $c = 12.876$  Å and  $a = 2.686$  Å,  $c = 4.306$  Å; for the rhombohedral and hexagonal phases, respectively) are in good agreement with those previously reported during the thermal decomposition of  $Ni_3C$  NPs [17], mechanically alloyed  $Ni_3C$  [23] and with theoretical calculations [18, 23]. The broad and low-intensity diffraction peaks indicate the formation of small sized entities.

In this regard, it is not possible to detect reflections corresponding to this  $Ni_3C$  phase in the samples synthesized at temperatures above  $400^\circ\text{C}$ , although regions containing a small number of coherent lattice planes with a lattice spacing corresponding to that of  $Ni_3C$  phase can be observed on HRTEM images (even for S600 sample, see below). The lack of X-ray diffraction peaks associated with  $Ni_3C$  phase together with the existence of a considerable background signal in the XRD patterns supports the idea that higher carbonization temperatures favour a high degree of disorder, and consequently a degradation of the long-range order in this Ni-rich phase. Similar behaviour was reported during the relaxation and crystallization under controlled annealing of  $Ni_{80}B_{20}$  metallic glass [41]: very small  $Ni_3B$  crystallites nucleate in Ni-rich regions with a high density of defects at the grain boundaries and surrounded by amorphous Ni phase not

permitting the establishment of long-range crystalline order [42].

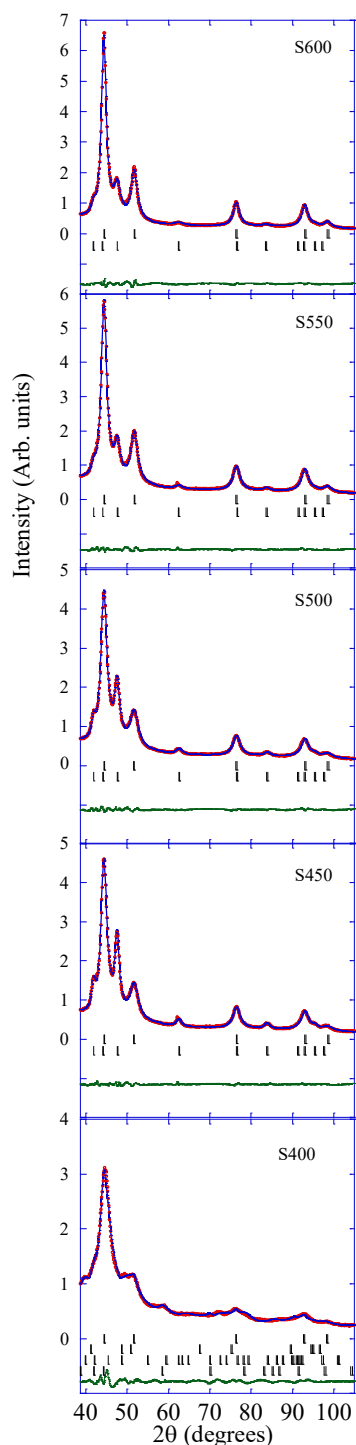


Fig. 1 Observed (red points) and calculated (blue lines) powder XRD patterns of the samples collected at room temperature. For samples S450 to S600 the first series of vertical bars correspond to the positions of the Bragg reflections associated with the crystal structure of Ni-FCC, and the second one with that of Ni-HCP. For sample S400 the vertical bars correspond to the positions of the Bragg reflections associated with the crystal structure of (from top to bottom) Ni-FCC, Ni-HCP, rhombohedral  $\text{Ni}_3\text{C}$ , and hexagonal  $\text{Ni}_3\text{C}$ . The observed-calculated difference pattern is depicted at the bottom of each figure.

On the other hand, considering the broadening of the diffraction peaks and using the procedure based on a generalized Scherrer-peak-broadening formula [35], it was possible to extract the corresponding sizes of the coherent diffraction crystallites. It is important to note the small diameter for the Ni NPs with FCC crystal structure (between 3.8 and 5.6 nm) compared to other Ni NPs systems [43]. This feature could be attributed to the presence of both  $\text{Ni}_3\text{C}$  and Ni-HCP phases covering the Ni-FCC cores that hinder growing up and sintering of the NP cores [16]. This circumstance will be of paramount relevance when explaining the magnetic properties of these Ni-based NPs (see below).

### Microstructure and morphology

Considering that the relative Ni content of the samples depends on the carbonization temperature at which the synthesis of the samples takes place (see Table 1), we may expect a change in the number and size of the Ni-NPs. In Figure 2 several TEM and HRTEM images are displayed, where Ni-NPs with quasi-spherical shape are randomly dispersed (dark spots in TEM images) within the carbon matrix. The histograms of the NP size distributions were obtained after measuring the diameter values of at least 300 isolated NPs from several TEM images, and then, fitting those histograms to a lognormal distribution function characterized by its mean diameter ( $D_{\text{TEM}}$ ) and standard deviation ( $\sigma$ ) (see Figure 3). These fits reveal a single broad distribution (ranging between 2-20 nm) for all samples with  $D_{\text{TEM}}(\sigma)$  values of 7(6) nm, 8(3) nm, 7(2) nm, 8(2) nm and 10(6) nm for S400, S450, S500, S550, S600, respectively (see Table 1).

Aiming to disentangle the complex mixture of crystalline phases identified from the XRD analysis and the carbonization temperature dependence of the evolution of those phases, we performed a careful HRTEM analysis for individual NPs in the samples S400, S450, S500, S550 and S600 that confirmed their crystallinity with observable lattice fringes in several crystallographic directions. Since there are crystallographic planes in Ni-FCC, Ni-HCP, hexagonal  $\text{Ni}_3\text{C}$  and rhombohedral  $\text{Ni}_3\text{C}$  crystals (namely (111), (011), (002) and  $(\bar{1}23)$ ), respectively, with  $d_{\text{hkl}}$ -spacing value  $\approx 2 \text{ \AA}$ , we can only, undoubtedly, distinguish these 4 crystalline structures using HRTEM analysis based on the presence of other sibling  $d_{\text{hkl}}$ -spacing corresponding to other related planes that can be attributed to only one crystallographic structure of those four. In Figure 4a, a HRTEM image of a NP in S400 sample is displayed in which only unidirectional lattice fringes could be clearly analysed, even after performing its autocorrelation function (see Figure 4b). Based only on HRTEM analysis, the observation of crystalline NPs with  $d_{\text{hkl}}$ -spacing values  $\approx 2 \text{ \AA}$ , with an absence of other analysable lattice fringes in other directions provide a statistical probability of 25% that these crystals could be attributed to Ni-FCC. However, relying on the statistical significance of Rietveld refinement of the XRD patterns, this sample should have around 10% of the NPs belonging to Ni-FCC.



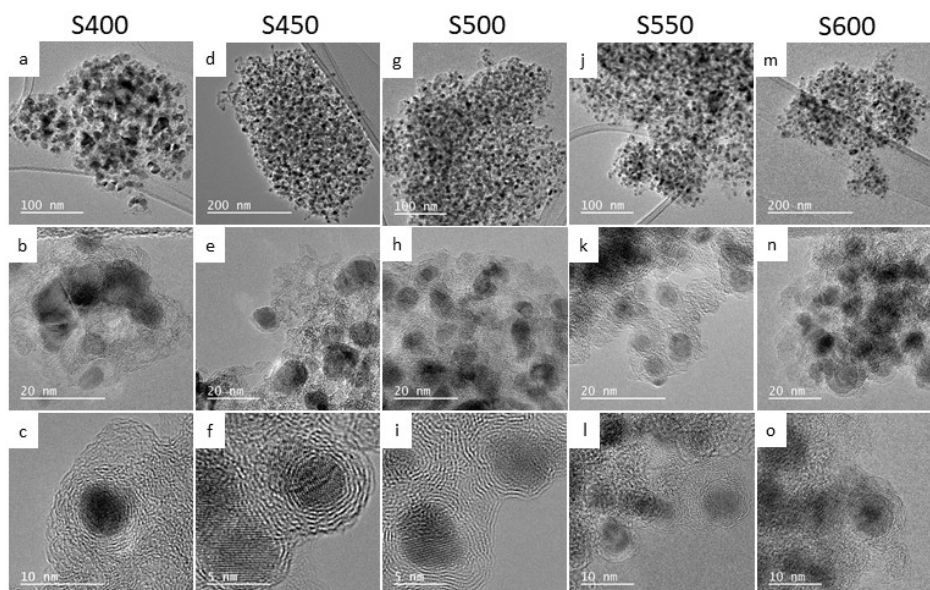


Fig. 2 Representative TEM and HRTEM images of samples (a-c) S400, (d-f) S450, (g-i) S500, (j-l) S550, (m-o) S600.

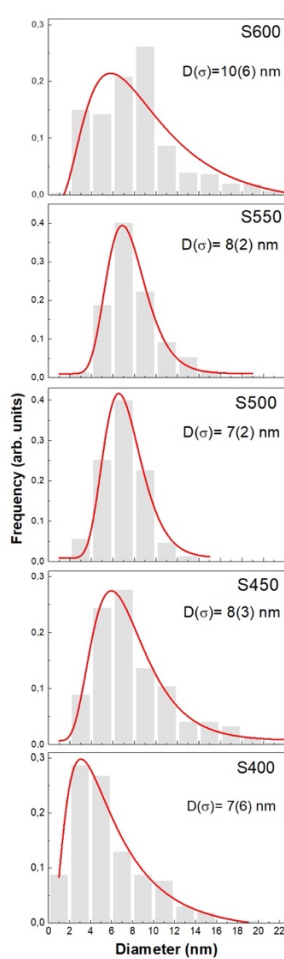


Fig. 3 Histograms of the total particle size distributions of the samples together with log-normal fits, providing mean diameters ( $D$ ) and standard deviations ( $s$ ).

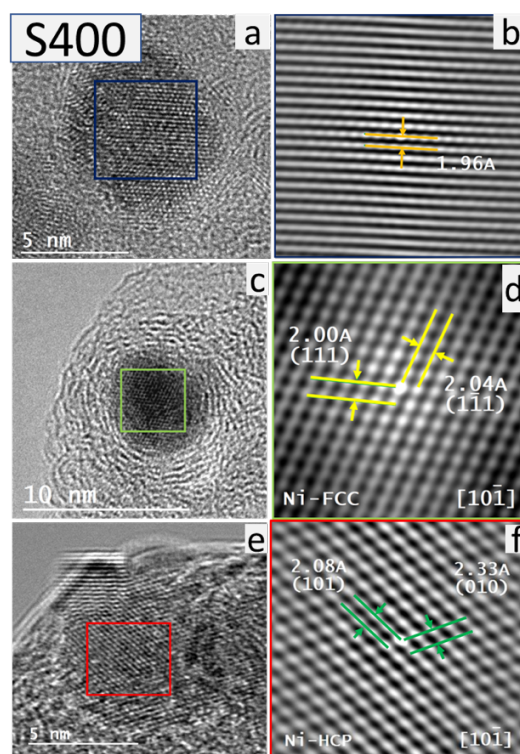


Fig. 4 HRTEM images for four representative NPs in the sample S400 (left column) and their analysed autocorrelation micrographs for the areas indicated by the coloured squares (right column). Analysing the NP displayed in (a) revealed lattice fringes in one direction (b) with  $d_{hkl}$ -spacing common between Ni-FCC, Ni-HCP, Ni-FCC and Trigonal  $Ni_3C$ . (c) At a specific defocusing for the NP, where it exhibits less image sharpness, crystallographic planes in the zone axis  $[10\bar{1}]$  for Ni-FCC could be identified (d). Other two crystallographic zones accounting for Ni-HCP could be detected for the NPs displayed in (e,f), zone axis  $[10\bar{1}]$  of Ni-HCP.



If this is the case, the existed Ni-FCC NPs could be difficult to be certainly identified, especially if they comprise the core of the NPs, since the microscopic resolution would be lacking under this defocusing imaging setting. Yet, with some defocusing, we could surely identify Ni-FCC crystallographic zones (Figures 4c & d). Other crystallographic structures easily distinguished in this sample were Ni-HCP (Figures 4e & f). For the S450 sample the HRTEM analysis confirmed on the continued existence of Ni-HCP and Ni-FCC (Figure 5).

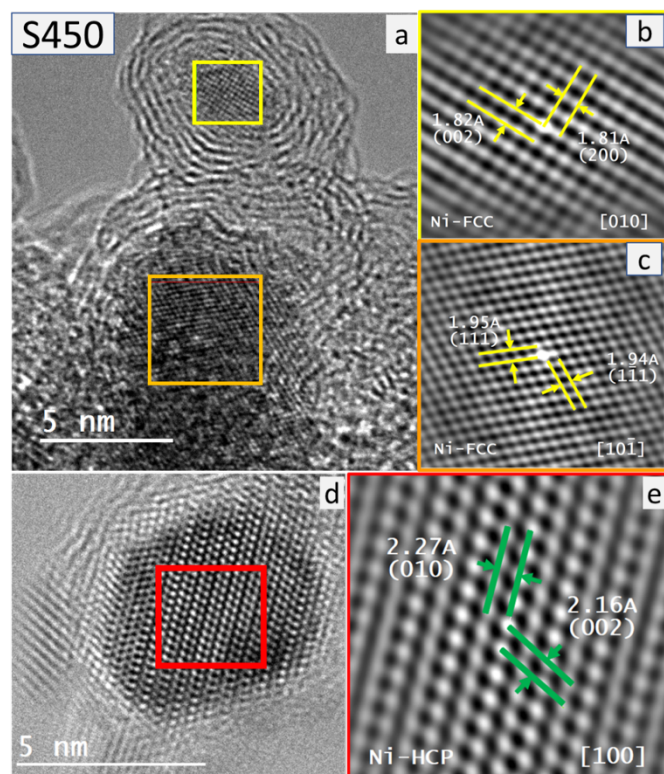


Fig. 5 Representative HRTEM images for three NPs in sample S450 (left) and their analysed autocorrelation micrographs for the areas indicated by coloured squares (right). (a) two NPs exhibiting relatively low image sharpness (defocused) and the analysis of their autocorrelation micrographs revealed crystallographic planes belonging to two zone axes: (b)  $[010]$  and (c)  $[10\bar{1}]$  accounting for Ni-FCC crystalline structure. (d) A nanoparticle displayed with high image sharpness (focused) revealed the crystallographic planes belonging to the zone axis  $[100]$  of Ni-HCP crystalline structure (e).

Worthy to mention here that the identified Ni-HCP crystallographic zones exhibit high image sharpness when compared to those of Ni-FCC. Further carbonization at 500 °C resulted in the growth of Ni NPs that undoubtedly account for the formation of cubic nickel nanocrystals (Ni-FCC) as was easily confirmed using the HRTEM images of the Ni NPs exhibiting multidirectional lattice fringes (Figures 6a & b). Furthermore, in the sample treated at carbonization temperature 550 °C, HRTEM images revealed both relatively less-sharp images with crystallographic zones attributed to Ni-FCC, beside the sharp images with crystallographic zones that undoubtedly accounted for Ni-HCP (Figures 6c to 6f). This could be attributed to the difference between the different (de-)focusing degrees

required to detect both polymorphs within a single nanocrystal, with Ni-FCC, most probably, occupying the nanocrystal cores (low-resolution crystallographic zones), while Ni-HCP occupying their outer shells (high-resolution crystallographic zones).

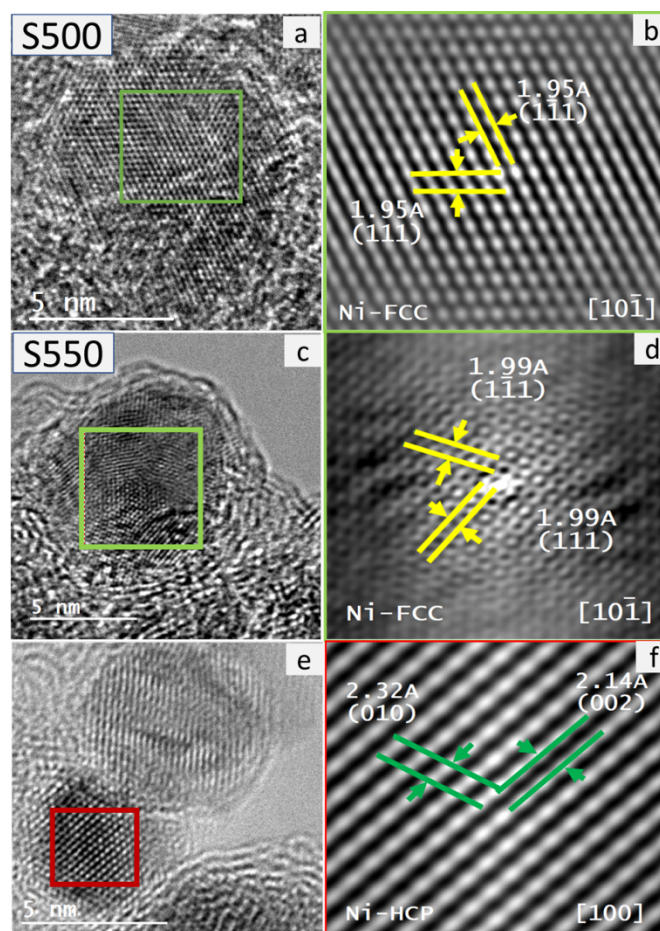


Fig. 6 Representative HRTEM images for three NPs in samples S500 and S550 (left column) and their analysed autocorrelation micrographs for the areas indicated by coloured squares (right column). (a) For S500, a nanoparticle displayed with high image sharpness (focused) and, (b) the analysis of its autocorrelation micrographs revealed crystallographic planes lying in the zone axis  $[10\bar{1}]$  that account for Ni-FCC crystalline structure. (c) For S550, a nanoparticle displayed with relatively low image sharpness was hardly analysed to reveal the crystallographic planes also in the zone axis  $[10\bar{1}]$  of Ni-FCC shown in (d). A NP imaged with high image sharpness (focused) revealed the crystallographic planes belonging to the zone axis  $[100]$  of Ni-HCP crystalline structure shown in (e) & (f).

This explanation was confirmed clearly for the Ni-NPs synthesized at the highest carbonization temperature used in the current study, 600 °C, as shown in figure 7. Besides, rhombohedral  $\text{Ni}_3\text{C}$  could be still detected in S600 sample (not shown). Therefore, it seems that, as a model picture, the NPs consist of a Ni-FCC core that changes to Ni-HCP in the outer region of the NP probably due to a hexagonal-type environment where a predominant  $\text{Ni}_3\text{C}$  phase is present (“artichoke-like” morphology consisting of successive Ni-HCP and  $\text{Ni}_3\text{C}$ -like “bracts” anchored to the Ni-FCC core).

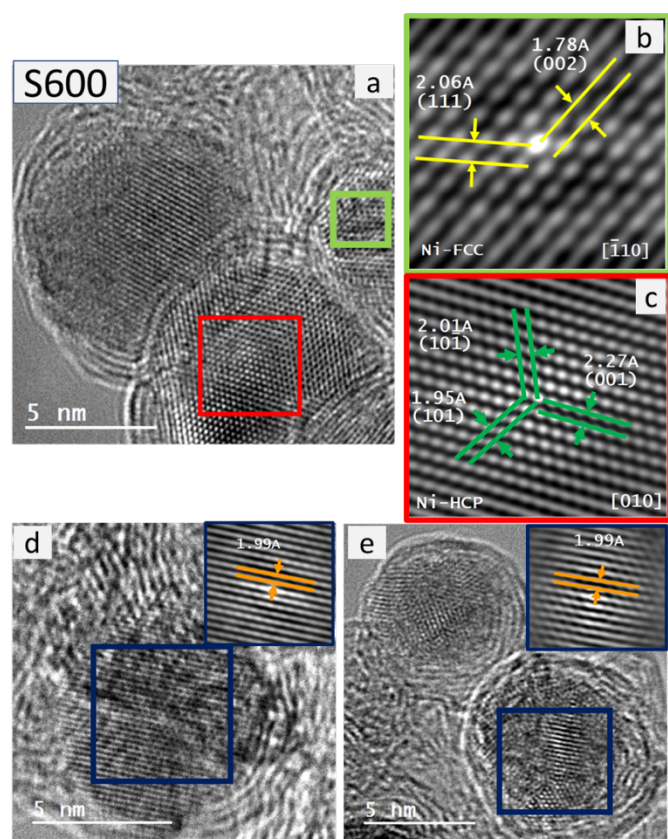


Fig. 7 Representative HRTEM images for three NPs in the sample S600 and their analysed autocorrelation micrographs for the areas indicated by the coloured squares. (a) Three overlapping NPs could be observed in this image, with the one indicated with the green square lying at a relatively higher focal plane (defocused) when compared to the other NP, indicated with red square, that lies in focus and thus shows high image sharpness. (b) The crystallographic analysis of the defocused NP revealed the crystallographic planes lying in the zone axis  $[\bar{1}10]$  of Ni-FCC crystalline structure, whereas; (c) the crystallographic analysis of the focused NP revealed crystallographic planes lying in the zone axis  $[010]$  of the Ni-HCP crystalline structure. (d,e) Other defocused (soft) HRTEM images of two NPs revealed unidirectional lattice fringes with  $d_{hkl}$ -spacing  $\approx 2\text{Å}$  that are most probably accounts for  $d_{111}$  of the Ni-FCC core of the resultant NPs.

Additionally, it should be mentioned that the HRTEM images of the samples show the turbostratic carbon layers around Ni-NPs, most likely due to the progressive transformation of the NiOF into a Ni metal-carbon composite (see Figure 2, bottom panel). This feature prevents the Ni-NPs from growing above 5-6 nm in diameter and protects these metallic Ni NPs from oxidation, as was confirmed by the absence of nickel oxide from either XRD and TEM/HRTEM analysis. Hence, we presume that the present synthesis procedure effectively facilitated the formation of relatively crystalline layers of turbostratic carbon covering most of the Ni-NPs (analogous to those recently found in Fe NPs [44]). This can be observed in Figure 8 for the sample S600, where an average distance of 0.35-0.36 nm between the stacked layers was measured. These findings suggest that the chemical synthesis route of the present work gives rise to a similar protection mechanism against NP oxidation to that already

achieved following a pyrolysis-based synthesis strategy using sucrose for carbon-coated Ni NPs [43].

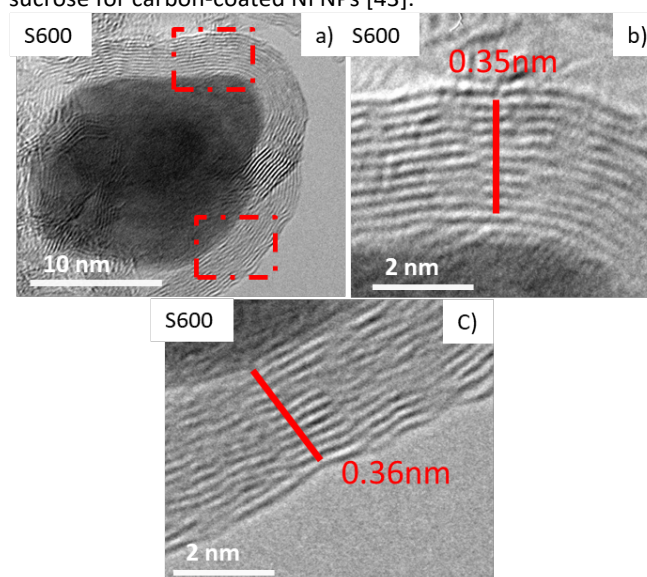


Fig. 8 The red dotted rectangles on the HRTEM image in a) represent regions where graphene-like concentric layers are clearly identified. The red lines in b) and c) show the stacking of the turbostratic carbon layers. (See text for more details).

### Magnetic behaviour

The magnetization versus the applied magnetic field,  $M(H)$ , curves measured at  $T = 300$  and  $5\text{ K}$  under ZFC conditions are depicted in Figure 9, and the values for the most relevant magnetic magnitudes obtained from the analysis can be found in Table 2. The  $M(H)$  curves at  $5\text{ K}$  are in fact hysteresis loops because they exhibit a non-zero coercive field ( $H_c$ ) and remanent magnetization ( $M_r$ ) related to the blocking of the spins in the NPs (see inset in Fig. 9b). The same  $M(H)$  curves have also been measured under FC conditions; however, no difference is observed compared with ZFC- $M(H)$  curves, hence, there is no existence of any exchange-bias effect as observed in other Ni-based nanoparticulate systems [45], and we can assume that only Ni-FCC contributes to the ferromagnetic signal (see below).

At  $T = 300\text{ K}$  the saturation regime for the magnetization ( $M_s$ ) is not yet reached under an applied magnetic field of  $50\text{ kOe}$  (see Fig. 9a), and the value of  $M_s$  estimated from the fit of the high applied field region ( $H > 30\text{ kOe}$ ) of the  $M(H)$  curves to a law of approach-to-saturation [46] increases with the carbonization temperature (see Table 2). It is worth noting that the sample with the smallest value for the  $M_s$  (S400) is that with the lowest percentage of Ni-FCC estimated from XRD patterns (see Table 1), slightly below 10%. If we assume that the Ni-FCC NPs possesses the value of  $M_s$  for pure Ni (58.6 and 55.1 emu/g at  $T = 5\text{ K}$  and  $300\text{ K}$ , respectively) and that this is the only phase contributing to  $M_s$  we reach to an estimated value for the percentage of Ni-FCC around 9%, which is in excellent agreement with XRD analysis. The  $M(H)$  curves for the other four samples display a much higher value (4 or even 5 times larger than that of sample S400) for the saturation



magnetization, thus suggesting a larger amount of Ni-FCC in S450, S500, S550 and S600, as previously obtained from XRD. Although some authors claim that Ni-HCP exhibits ferromagnetic behaviour [28, 29] with a magnetic moment similar to that of Ni-FCC, around  $0.6 \mu_B/\text{Ni}$  atom, the current magnetization data do not support such claim. In the case that both HCP and FCC Ni phases were ferromagnetic a much larger signal under an applied field of 50 kOe, will be expected for sample S400, what is contrary to our findings. Moreover, our investigation suggests that the presence of carbon atoms in a solid solution in Ni can not only stabilize the HCP crystalline structure for Ni, as was previously mentioned above, but concurrently, the coupling between the 3d-2p orbitals from the Ni-C bonding could establish a certain degree of covalence between these atoms, resulting in an antiferromagnetic or even non-magnetic character for the ground state of  $\text{Ni}_3\text{C}$  [23].

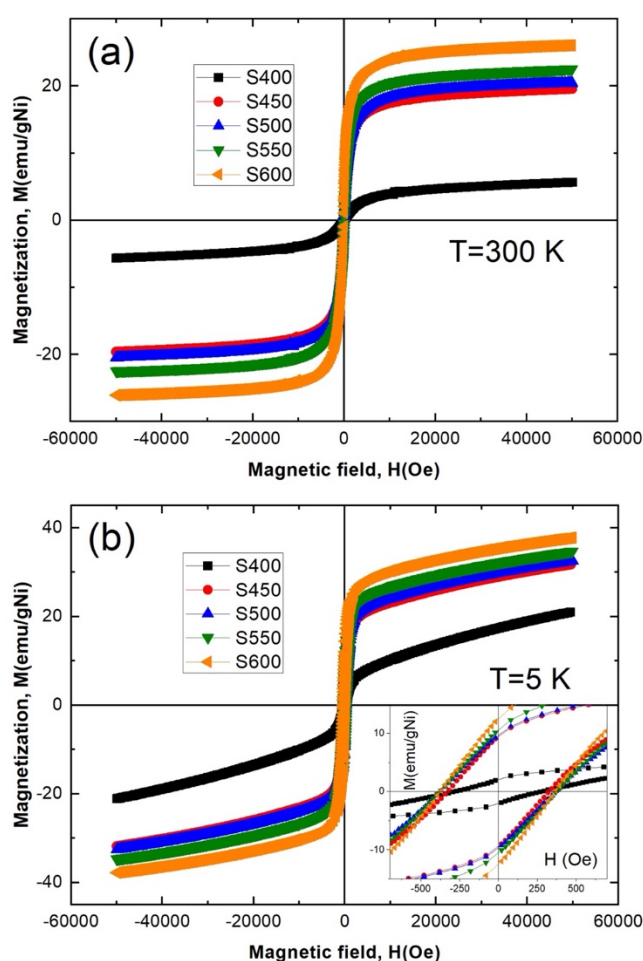


Fig. 9 Magnetization vs. applied magnetic field curves measured at  $T = 300 \text{ K}$  (a) and  $T = 5 \text{ K}$  (b). Note that insets show enlarged views of the origin region.

These ideas are strongly supported by the observation of a drastic increase in the slope of the low temperature  $M(H)$  curves measured at 5 K, far from being saturated (see Figure 9b). The latter clearly indicates a strong paramagnetic contribution coming from the other two phases detected from

both XRD and HRTEM experiments, namely,  $\text{Ni}_3\text{C}$  and Ni-HCP. Therefore, magnetization vs. applied magnetic field measurements reinforce the previously discussed argument about the influence of the carbonization temperature on the mixture and transformation of the different Ni-based crystalline phases that appear in these materials. Furthermore, the values obtained for the saturation magnetization of the samples synthesized at temperatures above  $400 \text{ }^\circ\text{C}$  are considerably smaller than those could be expected, considering the relative percentages between the Ni-FCC and Ni-HCP phases obtained from XRD analysis (see Table 1). The latter suggests that a significant amount of non-magnetic “dark-Ni” atoms is retained in a Ni-rich  $\text{Ni}_3\text{C}$ -like phase not detected by XRD due to the absence of long-range crystalline order but observed in HRTEM images as commented in the previous section.

Table 2. Values of the estimated blocking temperature and saturation magnetization. Note that the number in parentheses is the estimated error.

Sample	$T_B$ (K)	$M_s$ ( $T = 300 \text{ K}$ ) (emu/g)	$M_s$ ( $T = 5 \text{ K}$ ) (emu/g)
S400	15 (1)	4.7 (5)	4.9 (5)
S450	38	19.1 (5)	20.0 (5)
S500	40	20.2 (5)	21.1 (5)
S550	42	21.6 (5)	22.6 (5)
S600	50	25.2 (5)	26.4 (5)

In Figure 10 the evolution of the Ni containing phases is depicted as a function of the carbonization temperature. It must be noted that the values corresponding to the  $\text{Ni}_3\text{C}$  phase in samples S450 to S600 have been estimated from magnetic measurements and the relative percentage between Ni-FCC and Ni-HCP extracted from the analysis of XRD patterns, because only in the case of the S400 sample the percentage of this phase can be estimated from XRD as discussed above.

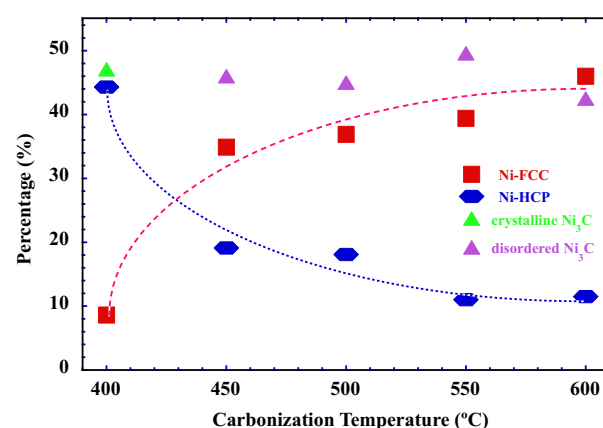


Fig. 10 Magnetization vs. applied magnetic field curves measured at  $T = 300 \text{ K}$  (a) and  $T = 5 \text{ K}$  (b). Note that insets show enlarged views of the origin region.

The temperature dependence of the magnetization,  $M(T)$  curves, measured following the ZFC and FC procedures between

$T = 5$  K and  $T = 300$  K under a magnetic field of 100 Oe is presented in figure 11.

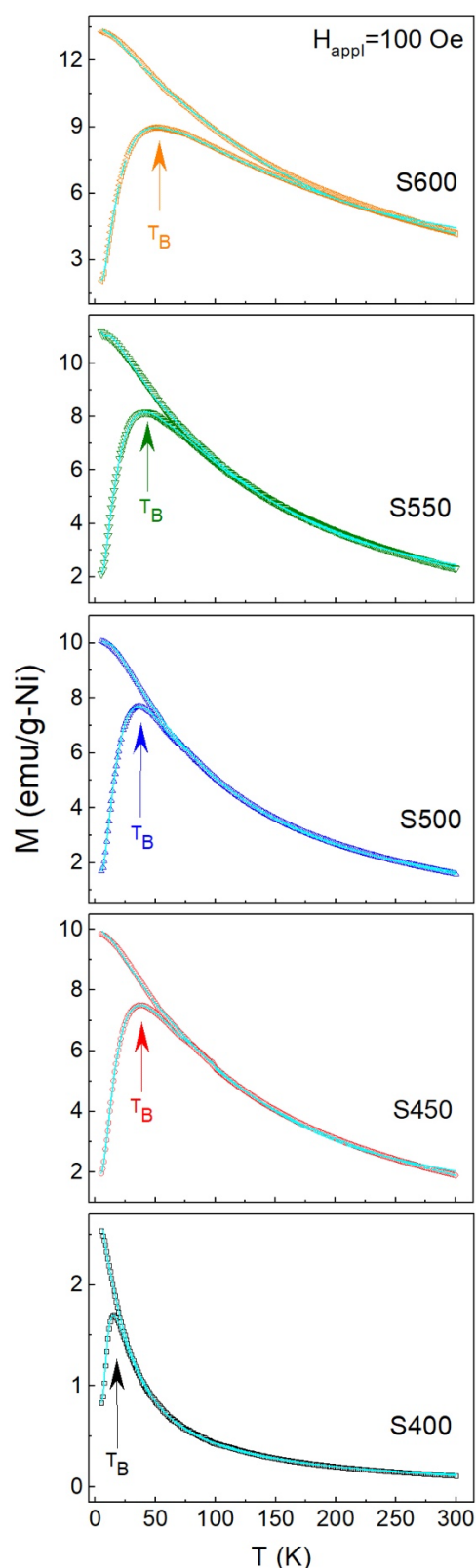


Fig. 11  $M(T)$  curves measured in the ZFC and FC regime under an applied magnetic field,  $H = 100$  Oe. The dots correspond to the experimental data, while the solid line is associated with the Stoner-Wohlfarth-based

fit. Arrows point out the average blocking temperatures ( $T_B$ ). (see text for details).

Even though the samples have different NP size distributions (see Figure 3), all of them present qualitative features typical of single domain ferromagnetic NPs that remain blocked below a certain temperature ( $T_B$ , blocking temperature) and behave as superparamagnetic (SPM) for  $T > T_B$ . The temperature for the maximum of the  $M_{ZFC}(T)$  curve is commonly ascribed to the average  $T_B$  of the system. Nevertheless, an increase of the NP average size gives rise to a shift of  $T_B$  towards higher temperatures and a wider temperature range for non-overlapping of  $M_{ZFC}(T)$  and  $M_{FC}(T)$  curves (irreversibility) that takes place at  $T = T_{irr}$ . Moreover, a broadening of the NP size distribution makes the maximum of the  $M_{ZFC}(T)$  curve less defined, since the NPs enter the SPM regime at a wider interval of temperatures depending on their size distribution profile.

The  $M(T)$  curves evidence a progressive evolution of the NP magnetic behaviour with the carbonization temperature. Sample S400 exhibits a canonical  $M_{ZFC}(T)/M_{FC}(T)$  variation with a well-defined and sharp maximum characteristic of non-interacting magnetic NPs (Figure 11) and an irreversibility temperature almost coinciding with the blocking temperature ( $T_{irr} \approx T_B$ ). The origin of this non-interacting regime could be ascribed to the “screening” effect provoked by the non-magnetic Ni-HCP and  $Ni_3C$  layers covering the Ni-FCC core spins. In contrast, the sample S600 displays a huge difference between  $T_{irr}$  and  $T_B$  (almost four times larger), suggesting that the decrease of non-magnetic Ni-based phases favours the magnetic coupling between the Ni-FCC NP spins. The samples synthesized at intermediated temperatures show a progressive change in the magnetic coupling (Figure 11).

Based on the Stoner-Wohlfarth model [47-49] we have refined the temperature dependence of the magnetization under ZFC/FC regimes (solid lines in Figure 8) using the NP size distribution obtained above (see Table 1 and Figure 3). The calculated curves are in excellent agreement with the experimental data, thus providing information about the magnitude and evolution of the effective magnetic anisotropy energy. While the bulk Ni-FCC has a value around  $10^6$  erg/cm<sup>3</sup>, the S400 sample is well below this value ( $\approx 10^4$  erg/cm<sup>3</sup>) and increases progressively to ca.  $10^5$  erg/cm<sup>3</sup> for the S600 sample. This difference can be explained by a change in the different (bulk, surface, and shape) contributions to the effective magnetic anisotropy, thus confirming the abovementioned change of physical regime, from non-interacting to interacting magnetic Ni-FCC NPs. This feature is clear evidence of the role played by the carbonaceous environment and the modification of the microstructure of the NPs produced as the carbonization temperature rises.

## Summary and conclusions

The investigated Ni nanoparticles embedded in a carbonaceous matrix represent a good example of the difficulty in determining the intricate relationship between structure and magnetism in multicomponent systems. Therefore, it appears highly necessary to develop cross checks between different

experimental techniques. An important characteristic of these complementary probes is not to introduce too much additional parameters beside those which are the relevant ones.

The main result of the current joint-analysis using X-ray diffraction, HRTEM analysis and magnetic measurements is that the carbonization temperature has not only a leading role on the amount of Ni, but also on the crystalline nature of the three coexisting phases (Ni<sub>3</sub>C, Ni-HCP and Ni-FCC), the formation of an exotic “artichoke-like” morphology, the size distribution of the nanoparticles, and their magnetic behaviour. In fact, for the sample S400 the Ni<sub>3</sub>C phase is almost certainly present in two different crystal structures, rhombohedral and hexagonal, with a major crystallinity. However, for carbonization temperatures above 400° C this Ni<sub>3</sub>C phase loses long-range crystalline order, becoming a sort of disordered solid solution in which Ni atoms are retained and do not contribute to the magnetization of the samples.

Additionally, it is worth noting the formation of several concentric turbostratic carbon layers covering the nanoparticles, which serve as a robust protection against nickel oxidation, contrary to what is seen in Ni-NP systems synthesized through conventional chemical routes that exhibit the typical Ni@NiO core-shell morphology, and the concomitant emergence of a magnetic exchange-bias effect. The last and most conceptually important point concerns the role of nickel-carbon interconnection in the physical-chemical properties of these nanoparticles. Our findings lead us to conclude that the present Ni@C hybrid introduces, not just some features that have to do with the protection against oxidation, but also features that promote the blockage of an important number of the Ni atoms, which therefore become non-magnetic, in contrast to what is usually seen for common metallic nickel. As a result, the present investigation based on a detailed and rigorous analysis of the magnetic data helps to understand the role that the different phases play in these Ni@C samples and could pave the way for the search of other Ni-based nanostructured systems in carbonaceous matrices that might be potentially used in a variety of technological applications.

### Author Contributions

M. F. performed some magnetic measurements and collected; she also carried out most of the data analysis and prepared the original draft of the manuscript. P. G., J.A.B. & J.I. P. & F.S.-G. were co-responsible of the conceptualization and methodology of the work. P. G., J.A. B., J.I. P. & J.P. A. were responsible for funding acquisition and supervision of the work. F.J. M.-J. synthesized the samples. D. M.-B. performed XRD experiments and contributed to data analysis. A. A. collected TEM/HRTEM images and performed the detailed analysis of the images. M.P. F.-G., J.H. B. and P. A.-A. were responsible for the analysis of the magnetic data. All the authors participated in the writing, review and editing of the final version of the manuscript.

### Conflicts of interest

There are no conflicts to declare.

### Acknowledgements

This work was supported by the Spanish MICINN, Agencia Estatal de Investigación (AEI) and the European Regional Development Fund (ERDF) through projects RTI2018-094683-B-C52 (Univ. Oviedo) & RTI2018-100832-B-I00 (INCAR-CSIC), as well as by the Plan de Ciencia, Tecnología e Innovación (PCTI) 2018-2022 del Principado de Asturias and the ERDF through projects AYUD/2021/51822 (Univ. Oviedo) and IDI/2021/000037 (INCAR-CSIC). A. Adawy acknowledges the financial support received from research projects MCI-21-PID2020-113558RB-C41 (MICINN) and GRUPIN-IDI/2018/170 (Principado de Asturias) to pursue her work at the Univ. Oviedo.

### Notes and references

- N.-D. Jaji, H.L. Lee, M.H. Hussin, H.M. Akil, M.R. Zakaria and M.B.H. Othman, *Nanotech. Reviews*, 2020, **9**, 1456.
- Z. Zhu, Z. Li, X. Wei, J. Wang, S. Xiao, R. Li, R. Wu and J.S. Chen, *Carbon*, 2021, **185**, 9.
- A. Dahal and M. Batzill, *Nanoscale*, 2014, **6** 2548.
- Z. Xiang, X. Zhang, Y. Shi, L. Cai, J. Cheng, H. Jiang, X. Zhu, Y. Dong and W. Lu, *Carbon*, 2021, **185** 477.
- P. Gorria, M. Sevilla, J. A. Blanco and A. B. Fuertes, *Carbon*, 2006, **44** 1954.
- M.R. Aghari, V. Soltaninejad and A. Maleki, *Sci. Rep.*, 2020, **10** 12627.
- H. Yan, Y. Dong, L. Cai, F. Pan and W. Lu, *Carbon*, 2022, **200** 317.
- B. Roldan-Cuenya, *Thin Solid Films*, 2010, **518** 3127.
- K.H. Oh, H.-K. Lee, S.W. Kang, J.-I Yang, G. Nam, T. Lim, S.H. Lee, C.S. Hong and J.C. Park, *J. Ind. Eng. Chem.*, 2022, **106** 449.
- B. Feng, R. Guo, Q. Cai, Y. Song, N. Li, Y. Fu, D.-L. Chen, J. Zhang, W. Zhu and F. Zhang, *Nano Res.*, 2022, **15** 6001.
- Y. Tian, Y. Liu, F. Pan, F. Wan and X. Zhang, *Colloids Surf. A: Physicochem. Eng. Asp.*, 2015, **464** 96.
- K. Shen, X. Chen, J. Chen and Y. Li, *ACS Catal.*, 2016, **6** 5887.
- M.Y. Zong, C.Z. Fan, X.F. Yang and D.H. Wang, *Mol. Catal.*, 2021, **509** 111609.
- M.H. Shahini, H.E. Mohammadloo, M. Ramezanzadeh and B. Ramezanzadeh, *Mater. Chem. Phys.*, 2022, **276** 125420.
- P. Gorria, M. P. Fernandez-Garcia, M. Sevilla, J. A. Blanco and A. B. Fuertes, *Phys. Status Solidi RRL*, 2009, **3** 4.
- F.J. Martín-Jimeno, F. Suárez-García, J.I. Paredes, A. Martínez-Alonso and J.M.D. Tascón, *J. Alloys Compd.*, 2021, **853** 157348.
- R.T. Chiang, R.K. Chiang and F.S. Shieu, 2014, *RSC Adv.*, **4** 19488.
- J.G. Wright and J. Goddard, *Philos. Mag.*, 1965, **11** 485.
- J. Gong, L.L. Wang, Y. Liu, J.H. Yang and Z.G. Zong, *J. Alloys Compd.*, 2008, **457** 6.
- A. Kotoulas, M. Gjoka, K. Simeonidis, I. Tsiaussis, M. Angelakeris, O. Kalogirou and C. Dendrinou-Samara, *J. Nanopart. Res.*, 2011 **13** 1897.
- Y.T. Jeon, J.Y. Moon, G.H. Lee, J. Park and Y.M. Chang, *J. Phys. Chem. B*, 2006, **110** 1187.
- Y. Goto, K. Taniguchi, T. Omata, S. Otsuka-Yao-Matsuo, N. Ohashi, S. Ueda, H. Yoshikawa, Y. Yamashita, H. Oohashi and K. Kobayashi, *Chem. Mater.*, 2008, **20** 4156.
- L. Yue, R. Sabiryanov, E.M. Kirkpatrick and D.L. Leslie-Pelecky, *Phys. Rev. B*, 2000, **62** 8969.

- 24 Z.L. Schaefer, K.M. Weeber, R. Misra, P. Schiffer and R.E. Schaak, *Chem. Mater.*, 2011, **23** 2475.
- 25 L. He, *J. Magn. Magn. Mater.*, 2010, **322** 1991.
- 26 Z. Xiang, C. Huang, Y. Song, B. Deng, X. Zhang, X. Zhu, D. Batalu, O. Tutunaru and W. Lu, *Carbon*, 2020, **167** 364.
- 27 S. Gao, G. Zhang, Y. Wang, X. Han, Y. Huang and P. Liu, *J. Mater. Sci. & Tech.*, 2021, **88** 56.
- 28 D.A. Papaconstantopoulos, J.L. Fry and N.E. Brener, *Phys. Rev. B*, 1989, **39** 2526.
- 29 X. He, L.T. Kong and B.X. Liu, *J. Appl. Phys.*, 2005, **97** 106107.
- 30 C.N. Chinnasamy, B. Jeyadevan, K. Shinova, K. Tohji, A. Narayanasamy, K. Sato and S. Hisano, *J. Appl. Phys.*, 2005, **97** 10J309.
- 31 M. Han, Q. Liu, J.H. He, Y. Song, Z. Xu and J.M. Zhu, *Adv. Mater.*, 2007, **19** 1096.
- 32 Y. Mi, D. Yuan, Y. Liu, J. Zhang and Y. Xiao, *Mater. Chem. Phys.*, 2005, **89** 359.
- 33 S. Fujieda, T. Kuboniwa, K. Shinoda, S. Suzuki and J. Echigoya, *AIP Adv.*, 2016, **6** 056116.
- 34 Y. Zhang, Y. Zhu, Y. Cao, D. Li, Z. Zhang, K. Wang, F. Ding, X. Wang, D. Meng, L. Fan and J. Wu, *RSC Adv.*, 2016, **6** 81989.
- 35 S. Fujieda, K. Shinoda, S. Suzuki and B. Jeyadevan, *Materials Transactions*, 2012, **53** 1716.
- 36 J. Rodriguez-Carvajal, *Physica B*, 1993, **192** 55.
- 37 D. Martinez-Blanco, P. Gorria, J.A. Blanco, M.J. Perez and J. Campo, *J. Phys.: Condens. Matter*, 2008, **20** 335213.
- 38 C.A. Schneider, W.S. Rasband and K.W. Eliceiri, *Nature Methods*, 2012, **9** 671.
- 39 N. Rinaldi-Montes, P. Gorria, D. Martinez-Blanco, A.B. Fuertes, L. Fernandez Barquin, J. Rodriguez Fernandez, I. de Pedro, M.L. Fdez-Gubieda, J. Alonso, L. Olivi, G. Aquilanti and J.A. Blanco, *Nanoscale*, 2014, **6**, 457.
- 40 N. Rinaldi-Montes, P. Gorria, A.B. Fuertes, D. Martínez-Blanco, Z. Amghouz, I. Puente-Orench, L. Olivi, J. Herrero-Martin, M.P. Fernandez-Garcia, J. Alonso, M.-H. Phan, H. Srikanth, X. Marti and J.A. Blanco, *J. Mater. Chem. C*, 2022, **10** 1798.
- 41 C. Ballesteros, A. Zern, A. Garcia-Escorial, A. Hernando and J.M. Rojo, *Phys. Rev. B*, 1998, **58** 89.
- 42 J.M. Rojo, A. Hernando, M. El Ghannami, A. Garcia-Escorial, M.A. González, R. García-Martínez and L. Ricciarelli, *Phys. Rev. Lett.*, 1996, **76** 4833.
- 43 M.P. Fernandez-Garcia, P. Gorria, M. Sevilla, M.P. Proença, R. Boada, J. Chaboy, A.B. Fuertes and J.A. Blanco, *J. Phys. Chem. C*, 2011, **115** 5294.
- 44 A. Ghogia, L.M. Romero Millán, C.E. White and A. Nzihou, *ChemSusChem*, 2022, e202201864.
- 45 N. Rinaldi-Montes, P. Gorria, D. Martinez-Blanco, Z. Amghouz, A.B. Fuertes, L. Fernandez Barquin, I. de Pedro, L. Olivi and J.A. Blanco, *J. Mater. Chem. C*, 2015, **3** 5674.
- 46 B.D. Cullity, *Introduction to Magnetic Materials*, Addison-Wesley, Reading MA, 2009.
- 47 M. Respaud, J.M. Broto, H. Rakoto, A.R. Fert, L. Thomas, B. Barbara, M. Verelst, E. Snoeck, P. Lecante, A. Mosset, J. Osuna, T. Ould Ely, C. Amiens and B. Chaudret, *Phys. Rev. B*, 1998, **57** 2925.
- 48 C. de Julián Fernández, *Phys. Rev. B*, 2005, **72** 054438.
- 49 K.L. Livesey, S. Ruta, N.R. Anderson, D. Baldomir, R.W. Chantrell and D. Serantes, *Sci. Rep.*, 2018, **8** 11166.



## GRAPHICAL ABSTRACT

